Rocksalt ZnMgO alloys for ultraviolet applications: Origin of band-gap fluctuations and direct-indirect transitions

I. Gorczyca [1,*] M. Wierzbowska [1] D. Jarosz [2] J. Z. Domagala [2] A. Reszka [2] D. Le Si Dang [3] F. Donatini,[3]
N. E. Christensen,[4] and H. Teisseyre [1,2,†]

[1]*Institute of High Pressure Physics, Polish Academy of Sciences, 01-142 Warsaw, Poland*
[2]*Institute of Physics, Polish Academy of Sciences, 02-668 Warsaw, Poland*
[3]*Université Grenoble Alpes, CNRS, Institute Néel, 38042 Grenoble, France*
[4]*Department of Physics and Astronomy, Aarhus University, DK-8000 Aarhus C, Denmark*

Rocksalt $Zn_xMg_{1-x}O$ alloys are theoretically and experimentally investigated for near- and deep-UV opto-electronics with a tunable band gap of 4.2–7.8 eV. Regarding the key question about the composition x, at which there is a transition between the direct and indirect gaps, we performed *ab initio* calculations for various Zn concentrations and all possible atomic arrangements in eight- to 64-atom supercells. We show that, depending on the detailed Zn distribution (clustered, random, or uniform distribution), the alloy band gap can vary by as much as 1.27 eV. The band gap is indirect for clustered and random Zn arrangements in the supercell. For uniform Zn arrangements, the gap is also indirect, except for $x < 0.5$ and atom uniform arrangements excluding Zn-O-Zn nearest neighbor bridges, for which the direct gap can be lowered below the indirect gap by about 0.1 eV. The mechanisms of band-gap fluctuation, Zn clustering, and direct-indirect band-gap transitions are analyzed and explained in terms of atomic contributions to band structures by projecting Bloch functions onto localized Wannier functions. Simultaneously, cathodoluminescence measurements were performed on a set of $Zn_xMg_{1-x}O$ multiquantum wells grown by molecular beam epitaxy on MgO substrates. We observed strong and broad emission bands, redshifting with increasing Zn concentration but featuring no clear-cut evidence for any direct to indirect band-gap crossover. We argue that these alloys are well suited for deep-UV optoelectronics, thanks to the rare combination of strong exciton binding energy, coupling to phonons, and carrier localization, which is favored by the marked flattening of the top valence bands by both short-range and long-range Zn-Zn interactions.

I. INTRODUCTION

Oxide semiconductors have attracted significant scientific and technological attention in the research community due to their unique combination of piezoelectric, electrical, and optical properties. Interesting physical properties of zinc oxide (ZnO), such as high transparency in the entire visible and ultraviolet (UV) regions and a wide range of conductivity, aroused interest toward applications in light emitters and detectors [1,2], chemical sensors [3], transparent thin-film transistors [4], multifunctional integrated circuits [5], and solar cells [6]. Oxides growth technology is well developed. High crystalline quality and high radiation resistance, as well as low cost, give oxides a competitive advantage over GaN based technologies. Epitaxial ZnO films of sufficiently high quality, much cheaper than GaN substrates, can be grown by various methods [7,8].

Unfortunately, due to the different: ZnO-wurtzite (WZ) and MgO-rocksalt (RS) crystallographic structures [9], available

from $Zn_xMg_{1-x}O$ films, emission energy is limited to 4.2 eV, which corresponds to the $Zn_xMg_{1-x}O$ band gap with 40% of Mg. For higher Mg contents, $Zn_xMg_{1-x}O$ films tend to be segregated into WZ and RS phases. On the other hand, promising for applications are RS $Zn_xMg_{1-x}O$ epilayers. They have band-gap energies between 4.2 eV (ZnO) [10] and 7.8 eV (MgO) [11] (the highest available nitride direct band gap is about 6.2 eV (AlN) [12]). RS $Zn_xMg_{1-x}O$ films were already grown on MgO (100) substrates by molecular beam epitaxy (MBE) retaining the RS crystal structure for $x \geqslant 0.17$, and the RS ZnO epilayer was stable up to 5 nm thickness [13]. As recently reported, RS $Zn_xMg_{1-x}O$ epilayers containing 2%–85% ZnO were successfully grown on MgO substrates and tunable band-gap energies of 6.2–4.5 eV were obtained for these structures [14]. They have potential use in optoelectronic devices operating in far-UV spectral ranges, with a broad range of applications in medicine [15], biology [16], chemistry, and materials science [17] (air and water purification, food preservation, air conditioners, currency screening, bioagent detection systems, and optical storage).

Despite the growing interest in RS $Zn_xMg_{1-x}O$ epilayers, measurements and calculations of the electronic properties of these heterostructures are still very scarce. Jaffe *et al.*

*iza@unipress.waw.pl
†teiss@ifpan.edu.pl

245202-1

[18] calculated the electronic band structure of RS ZnO using the all-electron local-orbital Hartree-Fock method. They predicted that RS ZnO has an indirect band gap, which is not useful for optoelectronic applications. Similar theoretical results were obtained by other researchers interested mostly in RS ZnO as a high-pressure phase of WZ ZnO. In addition, it remains unclear whether the RS ZnO phase is stable at ambient conditions. Unlike RS ZnO, RS MgO was predicted as a semiconductor with a direct band gap at ambient pressure; however, a 10% volume contraction shifts the conduction band minimum (CBM) from the Γ point to the X point [19]. Djelal *et al.* [20] reported density functional theory (DFT) calculations of the band structures of RS $Zn_xMg_{1-x}O$ alloys using 16-atom supercells. The authors suggested that the energy gap in this alloy is indirect in the entire composition range, $0 < x < 1$, except for MgO, where it is direct. Conversely, the theoretical work by Wang *et al.* [21] predicted direct gaps at $x = 0$, 0.25, and 0.375 and, surprisingly, indirect gaps at $x = 0.125$ and 0.5. Onuma *et al.* [22] reported data from cathodoluminescence (CL) measurements performed on a set of RS $Zn_xMg_{1-x}O$ films with $x = 0.61-0.92$ and compared them with *ab initio* band gaps calculated for RS $Zn_xMg_{1-x}O$ alloys. The authors emphasized the presence of E_g fluctuations caused by differences in the local distribution of Mg and Zn atoms in the alloy. However, it seems that their identification of the calculated band gaps as direct or indirect was not quite correct.

In the context of the aforementioned controversies and for future applications, it is crucial to clarify the real characteristics of the band gap in $Zn_xMg_{1-x}O$ throughout the entire range of composition and to understand the mechanism governing band-gap symmetry. To this aim, we performed band structure calculations for many compositions, x, and various Zn atomic configurations in eight- to 64-atom supercells. Calculations show that the spreads of the band gaps for chosen x exceed 1.25 eV depending on the choice of Zn sites. The valence band maximum (VBM) occurs at different high-symmetry points Γ, R, M, and X of the Brillouin zone (BZ). However, CBM is always located at the Γ point. Direct band gaps (Γ-Γ) rarely appear and only in some cases with $x < 0.5$, for atomic configurations in which Zn atoms are uniformly distributed in all crystal directions.

Discussing the mechanism of the fluctuations and direct-indirect band-gap transitions we characterized atomic contributions to the band structures via projections of the Bloch functions onto maximally localized Wannier functions (ML-WFs) [23,24]. We observed the influence of the Zn distribution on the shape of the valence band. In addition, the Hamiltonian matrix elements between MLWFs centered on chosen groups of atoms (Zn or neighboring O) and the dependence of these elements on the distance between Wannier centers give an estimate of the strength of the interactions between dopant atoms.

In order to compare our theoretical results with the experiment, CL measurements were performed on a set of $Zn_xMg_{1-x}O$ single quantum wells grown by MBE. In the last part of the paper, the experimental energy gaps estimated from these measurements were compared with the calculated band gaps.

II. METHODOLOGY

A. Theory

There exist different approaches to simulate alloys. The simplest one is the virtual crystal approximation (VCA), which averages all impurity configurations in the entire sample. Alternative to VCA is the much more advanced and one of the most used techniques, the "special quasirandom structure" (SQS) approach proposed by Zunger *et al.* [25,26] that mimics a perfectly random structure far better than the standard techniques. For the random substitutional alloys, the conventional band picture is broken due to the lack of translational symmetry. Fortunately, the approach proposed by Zunger and co-workers [27] can map the eigenvalues obtained from large supercell calculations into an effective band structure in the primitive cell, and can recover an approximate $E(k)$ for alloys.

The supercell method used in the present work can simulate a well uniform and clustered distribution of atoms, whereas the random distribution can be simulated only locally, inside the supercell. We simulate uniform, intermediate (locally random) as well as clustered configurations by constructing eight-, 16-, 32-, and 64-atom supercells, repeated "*ad infinitum*" in the band structure calculations. In such approach, due to periodicity, we are dealing in fact with the ordered alloy and we cannot construct the real random distribution of atoms. For each composition, x, we changed "by hand" the positions of the Zn atoms in the supercell. All the most clustered configurations (atoms grouped in one plane, or one corner of a supercell) lead to the same or very similar results for the band gap, so we presented only one representative case for each composition. In contrast, in the uniform configuration we tried to put the Zn atoms as far away from each other as possible, and again, we checked that all such configurations lead to very close values of gaps. Much more combinations are for intermediate cases leading to the "intermediate" values of the band gaps. We investigated many different distributions of atoms, excluding symmetrically equivalent. Some of them lead to very close values of the band gaps. In the manuscript we present several different values of band gaps for each composition, treating them not as "all possible," but rather as "examples."

The electronic band structures of ZnO, MgO, and $Zn_xMg_{1-x}O$ alloys were performed by self-consistent calculations based on the local density approximation (LDA) to density functional theory (DFT) with Perdew-Zunger parametrization [28] of the Ceperley-Alder exchange-correlation functional [29]. The values of total energies, atomic coordinates, and lattice parameters were determined using pseudopotentials as implemented in the Vienna *ab initio* simulation package (VASP) [30]. This code is well suited for calculations of the atomic relaxations in the entire supercell by minimizing the Hellman-Feynman forces.

The convergent results were obtained with an energy cutoff of 600 eV, and k-space integrations were performed by summing over a $5 \times 5 \times 5$ mesh of the Monkhorst-Pack special points [31].

Subsequently, the obtained relaxed atomic positions were used as input for the energy band structure calculations using

the linear-muffin-tin-orbital (LMTO) [32] method in the full-potential version [33]. A semiempirical correction procedure (LDA+C) [34,35] was used to account for the deficiency of LDA in predicting semiconductor gaps. The LDA+C adds external potentials, which peak sharply at the nuclear sites and therefore they push s states upward in the energy. This approach has been successfully applied in many systems based on III-V nitrides, their alloys, and superlattices (SLs) [36–46]. The LDA+C procedure not only corrects the fundamental gap, but also the dispersion of the conduction band and the gaps at other BZ points, performing well for bulk moduli, deformation potentials, and effective masses. It also works in the presence of an electric field [43]. The LDA+C method was originally developed and extensively applied in LMTO calculations [34–41,43], then in the linear augmented plane-wave (LAPW) framework [44,45]. Subsequently, it has also been applied to the pseudopotential method [46]. Potential parameters are specific for the atomic species and therefore transferable in the sense that they can be determined for two binary compounds and subsequently be applied to systems in which the compounds are combined, as in alloys, SLs, and heterojunctions. The parameters used in this work were determined separately for MgO and ZnO by adjusting to the values of the experimental gaps, and then applied to ZnMgO alloys. They were kept unchanged while the composition was varied. Our optimized values of the adjusting parameters are $V_0(\mathrm{Zn}) = 1000\,\mathrm{Ry}$, $V_0(\mathrm{Mg}) = 900\,\mathrm{Ry}$, $V_0(\mathrm{O}) = 800\,\mathrm{Ry}$, at the atomic sites, with the range parameter set to $r_0 = 0.015$ a.u. for all atoms. At all empty spheres we use $V_0 = 0.70\,\mathrm{Ry}$ and $r_0 = 0.60$ a.u. Further details on the calculations are given in Refs. [34,35].

In the second part of the calculations, the nature of electronic interactions responsible for the shape of the valence band in different atomic configurations was analyzed using the MLWFs [47,48]. Wannier functions were implemented in the code WANNIER90 [49]. We used this tool on top of the QUANTUM-ESPRESSO package [50]. Norm-conserving pseudopotentials with 12 electrons in the Zn valence configuration were used. A cutoff energy of 100 Ry for the plane-wave basis set was sufficient to obtain convergent results. The uniform mesh of the k points was set to $4 \times 4 \times 4$ for the supercell with 64 atoms and $8 \times 8 \times 8$ for the small cell with eight atoms.

The set of N Wannier functions $\omega_{n\mathbf{R}}(\mathbf{r}) = \omega_n(\mathbf{r} - \mathbf{R})$, $n \in [1, N]$ labeled by Bravais lattice vectors $\mathbf{R}$ may be constructed from a set of N Bloch bands $\Psi_{n\mathbf{k}}(\mathbf{r})$ as

$$|\omega_{n\mathbf{R}}\rangle = \frac{V}{(2\pi)^3} \int_{\mathrm{BZ}} \left[\sum_{m=1}^{N} U\big|_{mn}^{(\mathbf{k})} \big|\Psi_{n\mathbf{k}}\rangle \right] e^{-i\mathbf{k}\mathbf{R}} d\mathbf{k}, \quad (1)$$

where $U_{mn}^{(\mathbf{k})}$ is a unitary matrix. Different choices for $U_{mn}^{(\mathbf{k})}$ are possible and lead to the Wannier functions of varying spatial spreads. The Marzari-Vanderbilt method [23] of constructing the MLWFs is based on the minimization of the sum of the quadratic spreads:

$$\Omega = \sum_{n}^{N} [\langle \omega_{n0}|r^2|\omega_{n0}\rangle - |\langle \omega_{n0}|\mathbf{r}|\omega_{n0}\rangle|^2]. \quad (2)$$

The initial estimate for Wannier functions $\varphi_{n\mathbf{k}}(\mathbf{r})$ is made using the projections $A_{mn}^{(\mathbf{k})} = u_{m\mathbf{k}}|g_n$ of the Bloch eigenstates

onto the trial functions $g_n(\mathbf{r})$, usually the atomic shells and their hybridizations but not only, as follows:

$$\varphi_{n\mathbf{k}} = \sum_{m=1}^{N} A_{mn}^{(\mathbf{k})} |u_{m\mathbf{k}}\rangle. \quad (3)$$

Having found the transformation matrix $U_{mn}^{(\mathbf{k})}$, the Hamiltonian matrix can be represented based on the MLWF:

$$H_{mn}(\mathbf{R}) = \frac{1}{N_0} \sum_{\mathbf{k}} e^{-i\mathbf{k}\mathbf{R}} H_{mn}^{(\mathrm{W})}(\mathbf{k}), \quad (4)$$

where $H_{mn}^{(\mathrm{W})}(\mathbf{k}) = (U^{(\mathbf{k})})^{\dagger} H(\mathbf{k}) U^{(\mathbf{k})}$.

B. Experiment

The samples investigated in this study were grown by plasma assisted molecular beam epitaxy (PAMBE) (Riber Compact 21 system) on RS MgO (001) substrates from MTI Corporation. The system was equipped with a plasma cell as a gas source and standard effusion cells for group II elements. After chemical wet cleaning, MgO substrates were subjected to a pretreatment process, including an outgassing stage, which lasted for several hours at $700\,°\mathrm{C}$ in a buffer chamber. Finally, a 30-min oxidation in a growth chamber ($700\,°\mathrm{C}$) was performed. The growth was carried out at $460\,°\mathrm{C}$.

The grow rate 0.36 μm/h was measured *ex situ* after epitaxy by high-resolution transmission electron microscopy (HRTEM). A streaky pattern from the sample surface was revealed during and after the sample growth by reflection high-energy electron diffraction (RHEED).

Two types of samples were grown: single quantum wells (SQWs), and multiquantum wells (MQWs) with ten repetitions of $\mathrm{Zn}_x\mathrm{Mg}_{1-x}\mathrm{O}$ layers sandwiched between MgO buffers. In general, the samples were relatively thin. First, a 5–20-nm-thick MgO buffer layer was grown, and on the top of that the SQW or MQWs were grown with the thickness of 5–8 nm. Then, MgO barriers with the same thickness as the buffer layer and cap layer were grown. Regarding the concentration of $\mathrm{Zn}_x\mathrm{Mg}_{1-x}\mathrm{O}$ in the QWs region, we used the equation proposed in the recent publication by Wen *et al.* [14], who suggested that the content of ZnO in an epilayer can be expressed as

$$[\mathrm{ZnO}] := \mathrm{BEP}(\mathrm{Zn})k/[\mathrm{BEP}(\mathrm{Zn})k + \mathrm{BEP}(\mathrm{Mg})],$$

where BEP(Zn) and BEP(Mg) are beam equivalent pressures and $k = 0.265$. k is the experimental constant defined as $k = \gamma\mathrm{Zn}/\gamma\mathrm{Mg}$, where γx is the sticking coefficient of element x. In Ref. [14] it has been suggested that this experimental equation is valid over a fairly wide range of growth temperatures between $400°$ and $600\,°\mathrm{C}$. The analysis of experimental data on the Zn content in the epilayers presented in this work is based on x-ray energy dispersive spectroscopy (EDS), with accuracy estimated to be $\sim$1% for the alloy composition.

III. THEORETICAL RESULTS

A. Supercells, crystal symmetry, band folding

To examine the dependence of the RS $\mathrm{Zn}_x\mathrm{Mg}_{1-x}\mathrm{O}$ band gap on the composition and various Zn atomic arrangements, we performed the band structure calculations for eight-, 16-,
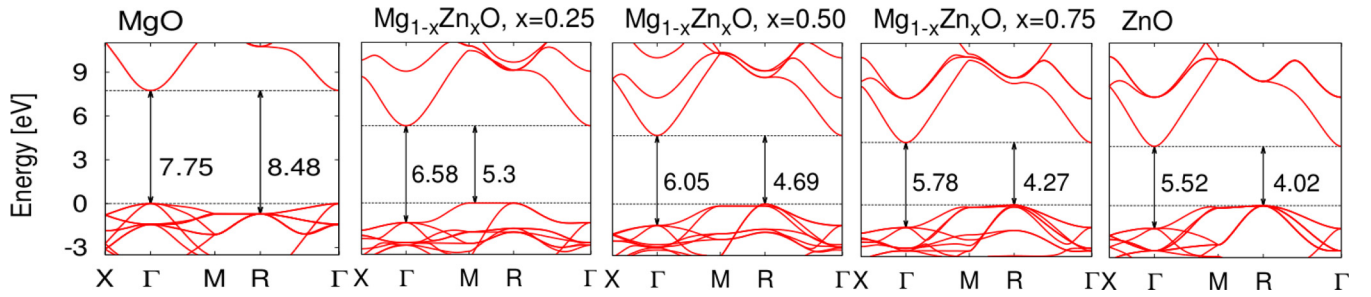
FIG. 1. The calculated band structures of RS $Zn_xMg_{1-x}O$ ($x = 0, 0.25, 0.5, 0.75$) in an eight-atom supercell. The Γ-Γ and R-Γ band gaps obtained from the LDA+C are provided in eV.

32-, and 64-atom supercells. For each composition we changed the positions of the Zn atoms in the supercell.

MgO crystalizes in the RS-B1 structure of NaCl, where each atom is sixfold coordinated and we assume this structure for RS $Zn_xMg_{1-x}O$ alloys. It is necessary to emphasize the difference between the RS-B1 structure and the eightfold coordinated RS-B2 structure [51] characteristic for the high-pressure phase (above 250 GPa) of ZnO. The authors of an earlier work [22] on RS $Zn_xMg_{1-x}O$ alloys compared their experimental results with the calculations performed for the B2 structure (Ref. [22], Fig. 4). Therefore, the differences between the assignment by us and these authors of the direct band gap may also result from the different, B1 and B2, structures.

The supercells constructed to simulate RS $Zn_xMg_{1-x}O$ alloys have the following symmetries: simple cubic (sc) for eight atoms, face-centered cubic (fcc) for 16 atoms, body-centered cubic (bcc) for 32 atoms, and sc again for 64 atoms. In particular, the high-symmetry W and L points of the Brillouin zone (BZ) in fcc symmetry correspond to the M and R symmetry points in the sc cells, respectively,

In the context of the direct-indirect band-gap problem, it is very important to pay attention to the band folding that occurs in the geometry of 16-, 32-, and 64-atom supercells. The energy bands at the high-symmetry points at the edges of the BZ are folded down to the Γ point due to the reduction of the BZ size (larger real cell means smaller BZ). For this reason, we denote the central point of the BZ as Γ', which means true Γ and all high-symmetry points X, M, and R of the larger reciprocal supercells that fold to Γ. To "unfold" the bands and identify them, we started with the eight-atom supercell (Fig. 1). In an eight-atom supercell (sc symmetry), the R point of the BZ is not folded to the Γ point, but it corresponds to the L point of the BZ in the original two-atom cell (fcc symmetry). We get exactly the same direct and indirect band gaps for binaries, ZnO, and MgO in two- and eight-atom cells. With this in mind, we followed folding of bands in larger supercells by comparing bands obtained in eight-, 16-, 32-, and 64-atom supercells for binaries and $Zn_xMg_{1-x}O$ alloys. At the end of this complicated process, at the Γ'-point, we identified the band energies originally belonging to other high-symmetry points.

Comparing our numerical results with the calculations by Onuma *et al.* [22] we found that the authors probably did not take into account the bands folding. Their lowest direct band gaps correspond to our lowest indirect gaps. On the other hand, their indirect gaps are indeed indirect and mainly correspond to the band gaps between lower-symmetry points

at the VBM (see plateau R-M in Fig. 1) and CBM at the Γ point. Another difference between their results and our calculations is the aforementioned difference in structures: (B2 in Ref. [22] and our B1).

B. Band-gap fluctuations, Zn clustering

At first, the band structures of RS $Zn_xMg_{1-x}O$ alloys are calculated in the eight-atom supercell geometry, for compositions $x = 0.25, 0.5, 0.75$ and for pure MgO ($x = 0$) and ZnO ($x = 1$). In this geometry there is only one possible Zn-atomic arrangement for any composition x. The results are presented in Fig. 1. Only pure MgO has a direct band gap at the Γ point. Starting from 25% of Zn, we get an indirect band gap between VBM at the R point and CBM at the Γ point; moreover, VBM is nearly degenerate at the M-R symmetry line and the highest occupied band at the Γ point is approximately 1.3 eV below the VBM.

The band alignment between the VBM of pure ZnO and MgO is 1.46 eV (calculated with respect to the $2s$ state of oxygen). This high value gives an expectation of how strong the valence rearrangement in the alloy would be.

RS $Zn_xMg_{1-x}O$ band gaps as functions of Zn content, x, obtained from the calculations for eight-, 16-, 32-, and 64-atom supercells are collected in Fig. 2(a). For each composition a very diffuse picture of the band-gap values E_g reflects various arrangements of the Zn atoms in the supercell. The biggest differences are in the concentration range of 25%–50%, and the spreads of E_g exceed 1.25 eV. As will be shown later, the lowest band gaps coincide with close Zn-atom arrangements, forming Zn-O-Zn linear bridges or Zn-O planes. This result resembles the effect of In clustering in InGaN and InAlN. For comparison, uniform and clustered InAlN band gaps are presented in Fig. 2(b). The effect of carrier localization at the nanoscale in InGaN alloy was also studied by Kent and Zunger [52]. Experimental evidence of Anderson localization induced by intrinsic alloy compositional disorder in InGaN/GaN QWs has recently been presented by Hahn *et al.* [53]. They observed variations in the emission spectra at distances as short as 5 nm, consistent with fluctuations caused by random compositional disorder. This intrinsic alloy feature can generate local fluctuations of potential, which can lead to the carrier localization and subsequent PL line broadening.

For discussion of the In clustering in InGaN and InAlN see Ref. [35]. Effect of Zn clustering will be discussed in more detail in Secs. III D and V.
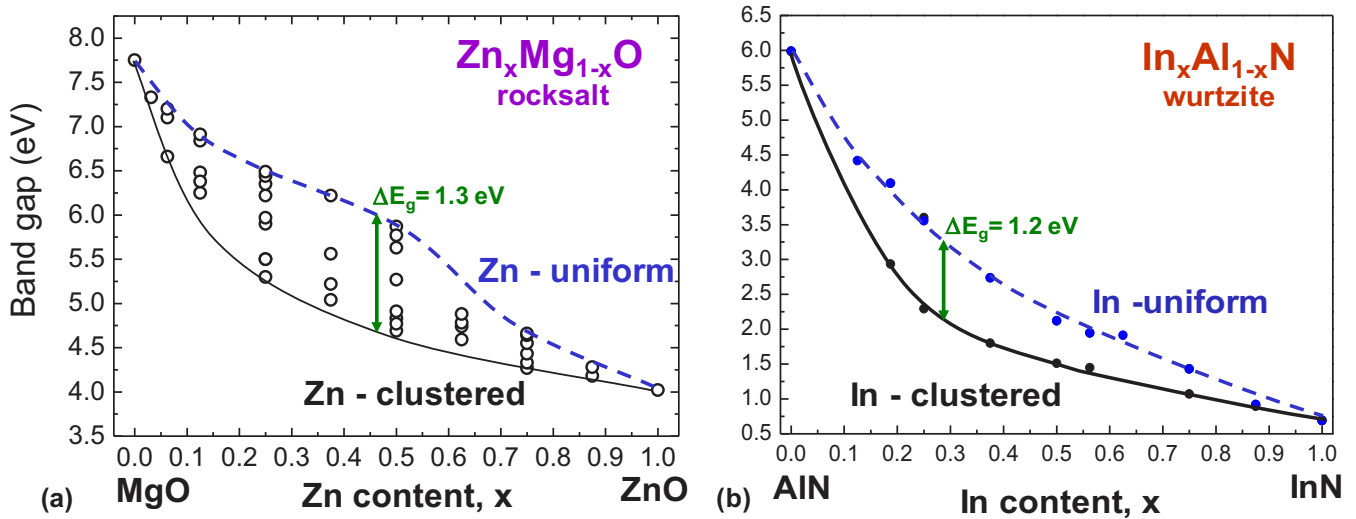
FIG. 2. (a) The calculated band gaps of RS $Zn_xMg_{1-x}O$ for various configurations using eight-, 16-, 32-, and 64-atom supercells. (b) Band gaps of wurtzite $In_xAl_{1-x}N$ from our earlier work on nitrides [38]. The solid black lines correspond to the lower limit of the gaps (clustered arrangement of atoms), and the dashed lines correspond to the upper limit of the band gaps (uniform arrangement of atoms). Arrows in (a), (b) indicate the band-gap spreading, ΔE_g, defined as the maximal difference between the band gaps obtained for clustered and uniform arrangements of atoms for the same composition, x.

C. Direct vs indirect band gaps

In addition to the fact that all band gaps in the eight-atom supercell (Fig. 1) are indirect (except for MgO), these gaps are the same as the lowest band gaps obtained for different atomic configurations in 16-, 32-, and 64-atom supercells [Fig. 2(a)]. Similarly, direct band gaps obtained in the eight-atom supercell are also the lowest direct gaps, considering all the possible atomic configurations. To illustrate this fact, Fig. 3 shows the indirect and corresponding direct band gaps calculated for eight-atom supercells and for larger supercells for various Zn arrangements. All these sets are a subset of the cases presented in Fig. 2. Figure 3(a) illustrates band gaps obtained using an eight-atom supercell—for which the arrangement of atoms is unique and corresponds to the clustered configuration. The same clustered configuration can be reproduced using larger supercells (16, 32, and 64 atoms) as shown in Fig. 3(b). In Fig. 3(c) we illustrate intermediate (locally random) arrangement of atoms; band gaps are obtained using 16-, 32-, and 64-atom supercells. The size of the supercell for uniform configuration of atoms should be as large as possible (we want them to be as far apart as possible). We took a 64-atom

supercell, but we checked the convergence by comparing the results with those obtained with 16- and 32-atom supercells. It happens that the differences are very small, especially between 32- and 64-atom supercells, but only in the case of a 64-atom cell do we get clear values of direct band gaps for $x < 0.5$, as indicated by the red line lying slightly lower than the black line representing the corresponding indirect transitions.

The mechanisms of band-gap fluctuations, effect of Zn clustering, and origins of direct-indirect gap transitions will be analyzed below and explained in terms of atomic contributions to the electronic band structure and lattice relaxation.

D. Atomic contributions to the valence bands, lattice relaxation

Electronic interactions responsible for the nature of the valence band are analyzed via projections of the Bloch functions onto MLWFs. For each chosen atomic configuration of two, four, eight, and 16 Zn atoms (composition, $x = 0.0625, 0.125, 0.25$, and 0.5) in the 64-atom supercell, illustrated in Fig. 4, a set of MLWFs centered at the Zn atoms is obtained. Since the
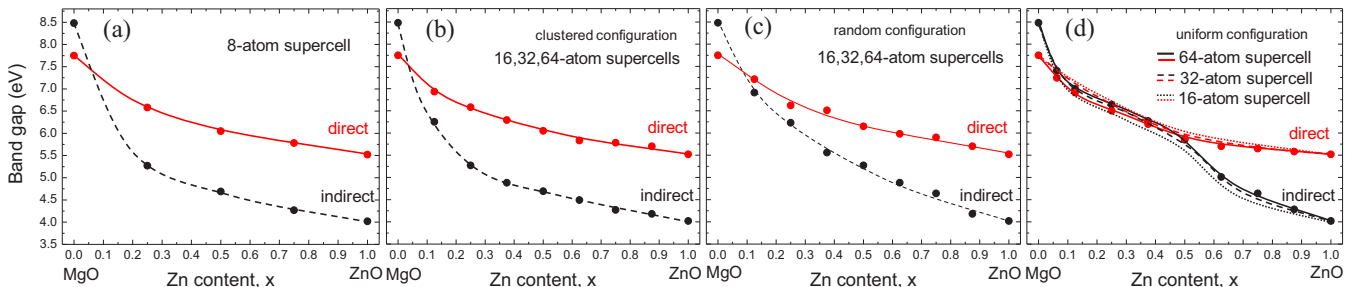

FIG. 3. The band gaps of RS $Zn_xMg_{1-x}O$ as functions of the Zn content x calculated using eight- (a) and 16-, 32-, and 64-atom supercells (b), (c), (d). In (b), (c), (d), the band gaps are presented for a few chosen Zn-atom arrangements in a supercell. The direct band gaps are indicated by red dots and red lines and the indirect band gaps are indicated by black dots and black dashed lines.
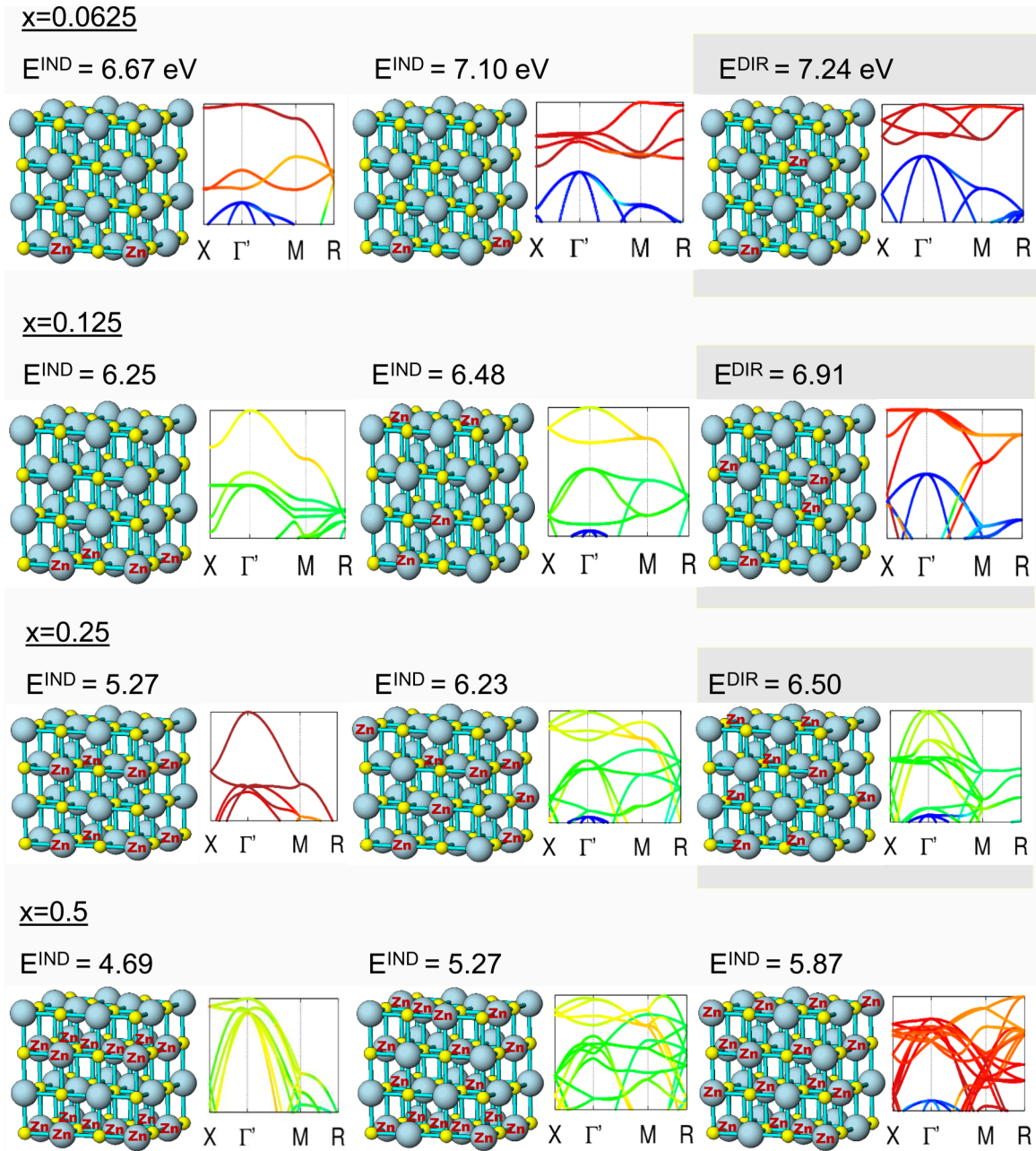
FIG. 4. The valence band evolution in 64-atom supercells. The composition x and the band-gap values with indication of their character (E^{DIR} or E^{IND}) are provided for each case. The direct band-gap cases are highlighted. Atomic colors: Mg—blue, O—yellow, Zn—blue with red labels. Color legends of the bands are projected onto the Zn-centered MLWFs. Blue represents an almost MgO-centered band and red signifies a high content of Zn in the band composition.

whole MLWFs set provides a complete basis for the Bloch function space, projection on a subset of MLWFs can only be a number from 0 to 1. Assessing the maximal values of the projection coefficients for all bands that did not exceed 0.3, we set the color legend in Fig. 4. High-symmetry points (R, M, X) are folded down to the center (denoted now by Γ') of the small BZ of the 64-atom supercell. Sets of three cases with different atomic configurations, from clustered to uniform arrangements of atoms, are provided for each composition.

Analyzing Fig. 4 we observe that the nature of the upper part of the valence band varies significantly depending on the Zn-atoms arrangement. We have found that VBM is built of MLWFs of Zn and oxygen atoms adjacent to Zn, in different proportions for each case. On the contrary, the VBM in pure ZnO is composed of oxygen-centered MLWFs without the contribution of a Zn atomic shell. The reason for the alloy's different behavior may be lower ionicity of the Zn-O bond compared with the Mg-O bond, with the charge density shifted toward Zn in the mixed compound. The covalency of Zn-O bonds increases with the degree of coordination of oxygen with Zn atoms and causes an increase in bandwidth. On the other hand, the CBM of pure ZnO is composed of Zn-centered MLWFs. Because both ZnO and MgO have a

CBM at the Γ point, the position of the CBM in $Zn_xMg_{1-x}O$ alloy does not vary.

Clustered configurations of Zn atoms presented in the first column of Fig. 4 are realized by linear Zn-O-Zn bridges and correspond to unique atomic patterns in a supercell with eight atoms, in which Zn atoms occupy positions along the [110] crystal direction for $x > 0.25$ or the [100] direction for $x = 0.25$. In a 64-atom supercell, the clustered configuration for $x = 0.0625$ can be realized by placing Zn atoms along the [100] direction (first case in Fig. 4). We note that the states at the VBM are separated from the rest of the valence bands. This separation occurs in cases with one or two Zn atoms in the supercell. However, VBM shows slight entanglement with other bands at the BZ corner (R point).

For the higher composition, $x = 0.125$, four Zn atoms are located in the corners of the square; for $x = 0.25$, eight Zn atoms are located in the corners of the cube; and for $x = 0.5$, 16 Zn atoms occupy the corners of two cubes, i.e., lie in the (100) planes as shown in the figure. All the above clustered configurations are characterized by very strong interactions between Zn atoms governed by couplings with adjacent oxygen atoms. Sixfold coordinated Zn opens the d shell and forms $sp3d2$ hybridization with neighboring oxygen. It involves the $d_{x^2-y^2}$ and d_{z^2} orbitals. This high coordination and specific hybridization leads to a very strong effect on the valence band top, pushing it up and leading to the lowest band-gap values. This is visible when the VBM position is compared with the maximum of the pure MgO-localized bands (blue bands in Fig. 4). We observe that the presence of Zn-dominated bands does not affect the shapes of MgO bands; only their distance to VBM varies, which is very clearly visible for the composition $x = 0.0625$.

Comparing to In clustering in InAlN and InGaN [35] we come to the conclusion that the role of the cation d shell is a common property of RS ZnO and WZ InN. Although tetragonally coordinated In does not open its d shell, this shell is energetically positioned very close to the Fermi level [54,55], which means that polarization effects can play a role in atomic clustering in In compounds.

In the middle column of Fig. 4 the Zn patterns that have a more diffuse distribution are illustrated. VBM is shifted lower toward the MgO bands, which leads to higher band-gap values. Also, we observe more entangled valence bands for higher compositions.

In the last column of Fig. 4 examples of uniform distribution of atoms are shown. The band-gap values are the largest and their character changes for compositions $x < 0.5$ from indirect to direct (highlighted cases). The VBM in the direct band-gap cases is found at the Γ point with a nearly degenerated X point in some cases.

The clustered configuration of atoms is accompanied by strong lattice relaxation. The shortest Zn-O relaxed bond lengths for clustered cases are listed in Table I in comparison with the shortest Zn-O bond lengths for uniform cases. Differences in the band-gap values, ΔE_g and in total energies, and ΔE_{tot} between clustered and uniform cases are also given.

In uniform atomic arrangements, we observe almost no changes in the bond lengths compared to the binary ZnO (2.111 Å) and MgO (2.072 Å) compounds, while in clustered alloys Zn-O bonds are up to 5% shorter than in ZnO. The ef-

TABLE I. Zn-O bond lengths in clustered and uniform arrangements of atoms and the corresponding differences in band gaps, ΔE_g, and in total energies, ΔE_{tot}, between both cases.

Composition x	Bond lengths (Å) clustered	Bond lengths (Å) uniform	ΔE_g (eV)	ΔE_{tot} (eV)
0.0625	2.041	2.085	0.57	–0.08
0.125	2.027	2.088	0.66	–0.23
0.25	2.009	2.092	1.23	–0.67
0.5	1.992	2.103	1.18	–1.34

fect is more pronounced for higher compositions, x, which coincides with the higher ΔE_g values of the band-gap reduction. The shorter bond length is the larger difference between the band gaps in clustered and uniform cases. Shortening of the bond lengths increases the strength of Zn-O-Zn interactions and leads to an even stronger hybridization of wave functions. As can be seen from Table I, the uniform configuration of atoms is the most stable, and this statement is valid also for other compositions, not included in the table. This means that direct band gaps that have appeared for such an arrangement of atoms can be preferable. However, the differences in total energies (the largest for $x = 0.5$) are not very large.

We have to point out that our intermediate configurations (between clustered and uniform configurations) are only locally random, due to periodicity and relatively small size of supercells. Nevertheless, we believe that the conclusion that band gaps for locally random distribution of atoms are lying above the gaps for clustered and below the ones for uniform configurations is valid also for real random configurations. Similar results were obtained previously for nitride alloys [35,38]. Also, Kent and Zunger [52] studying the effect of carrier localization in cubic InGaN obtained emission energies reduced by 200–300 meV compared to a random alloy as a consequence of In segregation.

E. Interatomic interaction strength at the short and long distance: Wannier analysis

Another demonstration of the long-range interactions governing the band structures of various Zn-doping patterns can be an analysis of the Hamiltonian matrix elements between the Bloch functions at a given k point in the reciprocal space or, equivalently, between the MLWFs in direct space; see Eq. (5) in Sec. II A. Since the pure ZnO in the wurtzite structure is a covalent system with the $sp3d2$ Zn hybridization (akin to that of the well reported BaTiO3 [56]), the Zn atoms embedded in the ionic MgO crystal will introduce new chemical bonds, which we analyze via the projections at the s and d shells of Zn and the $sp3$ lobes of O. This will show how the covalency of the Zn-O bond precipitates into the ionic system.

Additionally to the long-range interactions, we visualize the shorter-range interactions between Zn atoms in a more intuitive way. Figure 5 shows a plot of the real space representation of s-type Zn-centered MLWFs for several supercells. Only one MLWF centered on the selected Zn atom is plotted in each supercell, for visual clarity, and the other Zn atoms
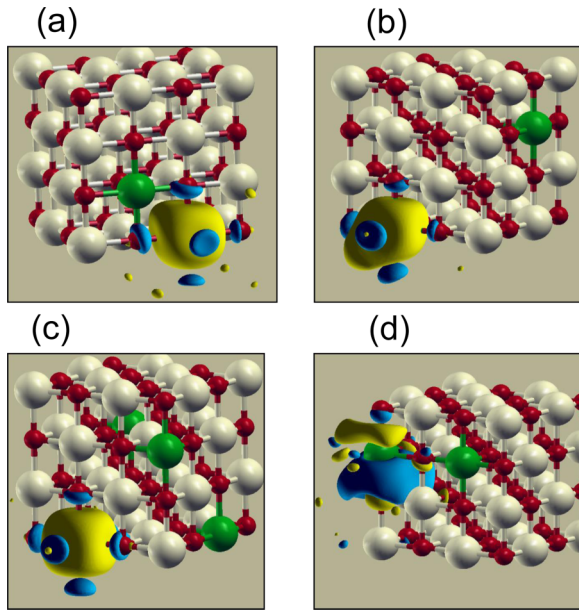
FIG. 5. Visualization of the *s*-type MLWFs (yellow and blue lobes) centered at one of the Zn atoms (in green) in the 64-atom supercells with various *x* concentrations and doping patterns: (a) Zn-Zn in (101) distance in the units of Zn-O bond; (b) Zn-Zn in (2,0,1) distance; (c) Zn-Zn in (2,2,0) distance; (d) Zn-Zn in (2,0,0) distance.

possess the symmetric functions. A variety of MLWF shapes illustrate different kinds of Zn bonds.

We can distinguish three types of bonds:

Polarized—Figs. 5(a) and 5(b)—the Zn bond is directed toward the adjacent Zn atom.

Symmetrical—Fig. 5(c)—refers to the case when the Zn atom has no adjacent Zn atoms, and farther Zn neighbors are distributed symmetrically.

The so-called "banana bond" or "bent bond" [57]—Fig. 5(d)—direct bond between Zn atoms with exclusion of oxygen atoms. The lobes of Wannier functions connect Zn atoms not along the shortest distance and straight line between them, but they bend avoiding the atom between them.

The banana bonds, or bent bonds, were found by Linus Pauling in 1931 [58], and because of their importance he was awarded a Nobel Prize in 1954. Thanks to this concept, it was possible to better predict the molecular or crystal structures. Further developments of this chemical-bonding type brought the Nobel Prize in 1976 to William N. Lipscomb for his studies of boranes [59]. The existence of the banana bonds in our system is a signature of the local covalency introduced by Zn atoms into ionic MgO. These bonds are markers of the tendency of atoms to form clusters, because the Zn-Zn interactions are strengthened by two contributions: (i) straight bonds mediated by O atoms (aforementioned highest contributions to the Hamiltonian, reported in Fig. 6) and (ii) additional direct bonds [reported in Fig. 5(d)] omitting the atoms which are residing at the Zn-Zn line.

IV. EXPERIMENTAL RESULTS

The key problem in growing ZnMgO MQW structures on MgO substrates is to determine the conditions for maintaining the RS phase. It was found that the maximum layer thickness of $Zn_xMg_{1-x}O$ strongly depends on the Zn concentration, decreasing with *x*, which reflects the phase instability of the alloy. In our case, we were able to grow a 3-nm ZnO QW (purely in the RS phase), sandwiched between two MgO layers. In a 10-nm-thick ZnO QW sample grown under the same conditions, HRTEM revealed a dominant RS phase, with mixed RS and WZ phase in some regions.

Our experimental results are consistent with previously published results by Lu *et al.* [13], where the authors suggested that 5 nm is a critical thickness for RS phase stability in ZnO/MgO structures. It is also worth noting that this value (5 nm) was used by us as a critical thickness that cannot be exceeded during SQW growth. Of course, as indicated in Ref. [13], for increasing MgO concentration, the critical thickness increases, reaching 130 nm for the $Zn_{0.5}Mg_{0.5}O$ layer.

High-resolution x-ray diffraction (HRXRD) studies of 002 (symmetrical) and $-1-13$ (asymmetrical) reflections were performed for our MQW's samples (Fig. 7). The chemical composition and thickness of the layers vary from sample to sample. However, from $2\theta/\omega$ scans—measured over a wide angle range (15°–120°)—it was confirmed that we observed a very small amount of WZ phase, at the level of 0.1%. Diffraction curves [Fig. 7(a), reflection 002, $2\theta/\omega$ scans collected with analyzer] show a series of maxima. Their angular positions (2θ scale) are associated with Bragg angles for constructive x-ray interference from $Zn_xMg_{1-x}O/MgO$ double layers repeated 10 times. Diffraction patterns with satellite peaks and dense oscillations between them confirmed the very high quality of the structures, with sharp interfaces between the MgO and $Zn_xMg_{1-x}O$ layers. In addition [Fig. 7(b), sample $Zn_{0.41}Mg_{0.59}O/MgO$, is representative of all other structures), from the reciprocal space map of the $-1-13$ reflection we received information that our structures are fully strained to the MgO substrate.

After the structural characteristics CL structural measurements were performed. The CL setup is an additional, internally developed system, mounted on the FEI Inspect F50 emission electron scanning microscope. The electron beam energy and current were set to 1 keV and 400 pA, respectively, and the area of $10 \times 10 \ \mu$m was scanned during 10 s, needed for spectral acquisition. The spectra were obtained using a Horiba iHR 550 spectrometer with an entrance slot width of 1 mm and acquired with the Andor Newton DU940 BU2 charge-coupled device (CCD) camera. Accelerating voltage was kept low to ensure "surface" pumping of our structures and minimize a contribution from the MgO substrate.

The room-temperature CL spectra of RS ZnMgO/MgO MQWs are shown in Fig. 8. They have two broad bands whose dependence on the Zn concentration is very different: a high-energy band with FWHM~0.8 eV, which monotonically shifts to lower energy as *x* increases, and a low-energy band at ~3.5–4 eV, FWHM > 1 eV, which shows chaotic behavior in both intensity and energy. Similar low-energy bands are also observed in CL spectra in Refs. [22,60]; most likely they are
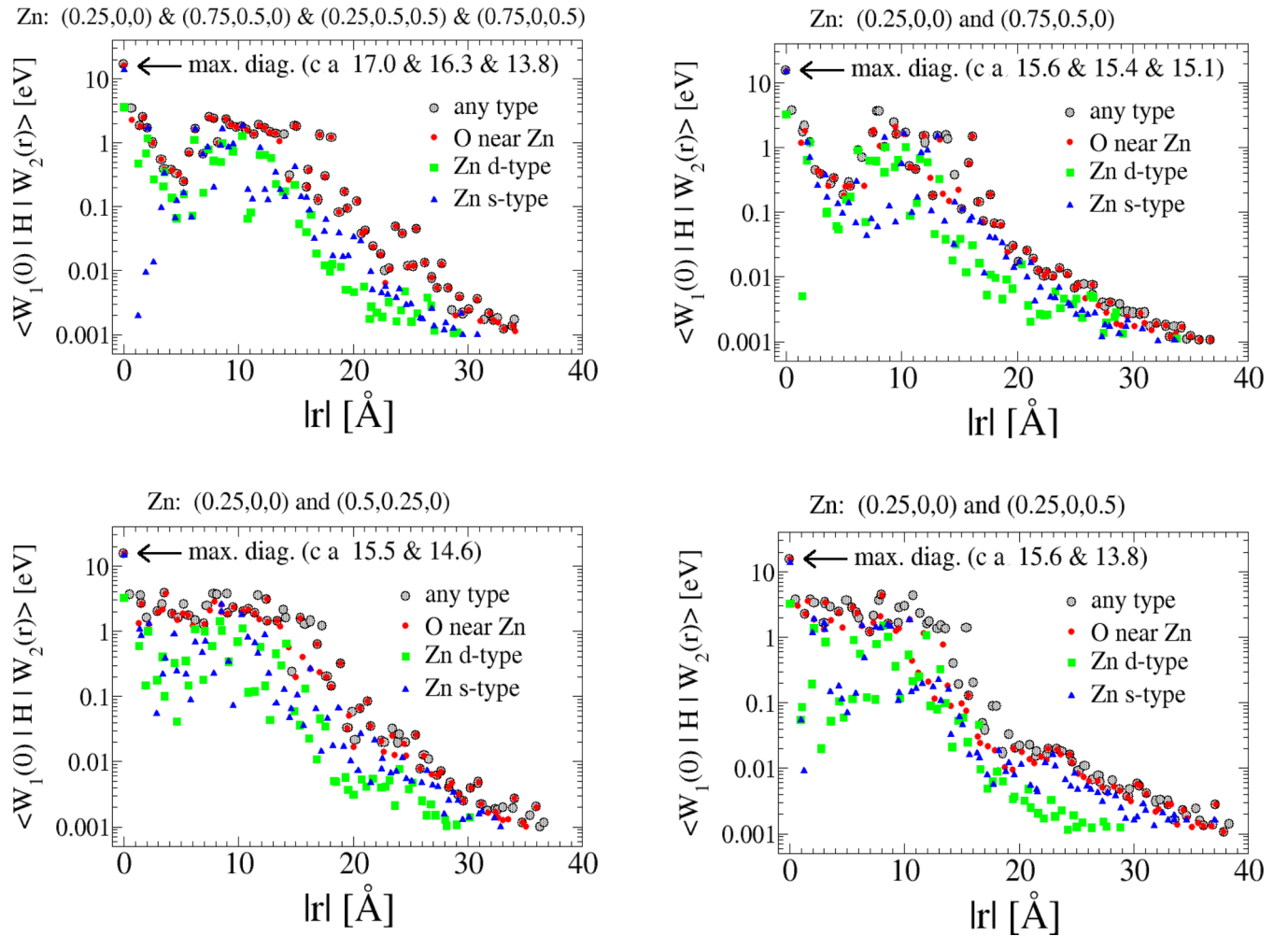
FIG. 6. The largest matrix elements of the Kohn-Sham Hamiltonian between the maximally localized Wannier functions (MLWFs) separated by the distance $|\mathbf{r}|$ in $Zn_xMg_{1-x}O$. The Wyckoff positions of the Zn atoms in the 64-atom supercells are shown above the corresponding plots. The MLWFs centers used for the projections of the Hamiltonian are marked with different colors. The maximal diagonal elements are pointed with arrows and their values are given explicitly.

associated with some defects that have not yet been identified in the epitaxial layer and will not be discussed further in this work. We assign high-energy bands to radiative recombination of excitons confined in MQWs.

V. COMPARISON BETWEEN EXPERIMENT AND THEORY

In Fig. 9 the obtained emission energies as functions of Zn concentration, together with other experimental results from the literature, are compared with the results of our calculations. Our experimental points are black; red points correspond to other published emission and absorption energies measured on ZnMgO epitaxial films grown on MgO (001) substrates by CVD, metal organic chemical vapor deposition (MOCVD), and MBE [14,22,60–62].

Solid blue lines represent theoretically obtained low-energy limits (clustered distribution of atoms) and high-energy limits (uniform distribution of atoms) of the indirect band gap [see Fig. 2(a)]. The green dotted line represents the fit to the lowest values of the obtained direct gaps.

Examination of Fig. 9 brings in the following remarks:

(i) Experimental data are strongly scattered but nevertheless lie within the two extreme limits of the theoretical indirect band gaps and below the lowest direct band gap. The lowest measured gaps are CL data in Ref. [22] which follow the theoretical "clustered" band gaps. These authors noticed that there is an important Stokes shift ∼0.7–0.8 eV between the CL bands and the optical transmission spectra in their samples. Taking this Stokes shift into account, it would shift their CL data upward, overlapping with our CL data and the optical transmission data of Wen *et al.* [14] and Choopun *et al.* [9] (not presented in Fig. 9 for clarity). On the other hand, the highest gaps extracted from x-ray photoelectron spectroscopy (XPS) [60] are close to the theoretical "uniform" gaps. XPS is certainly well suited to determine valence band edges. However, extending its use to obtain the band gap requires the implicit assumption of resonance between the Fermi level and the conduction band edge, which is not always justified.

(ii) The large FWHM ∼800 meV of our CL bands (Fig. 8) suggests radiative recombination of localized carriers (see further discussion below), which usually results in emission
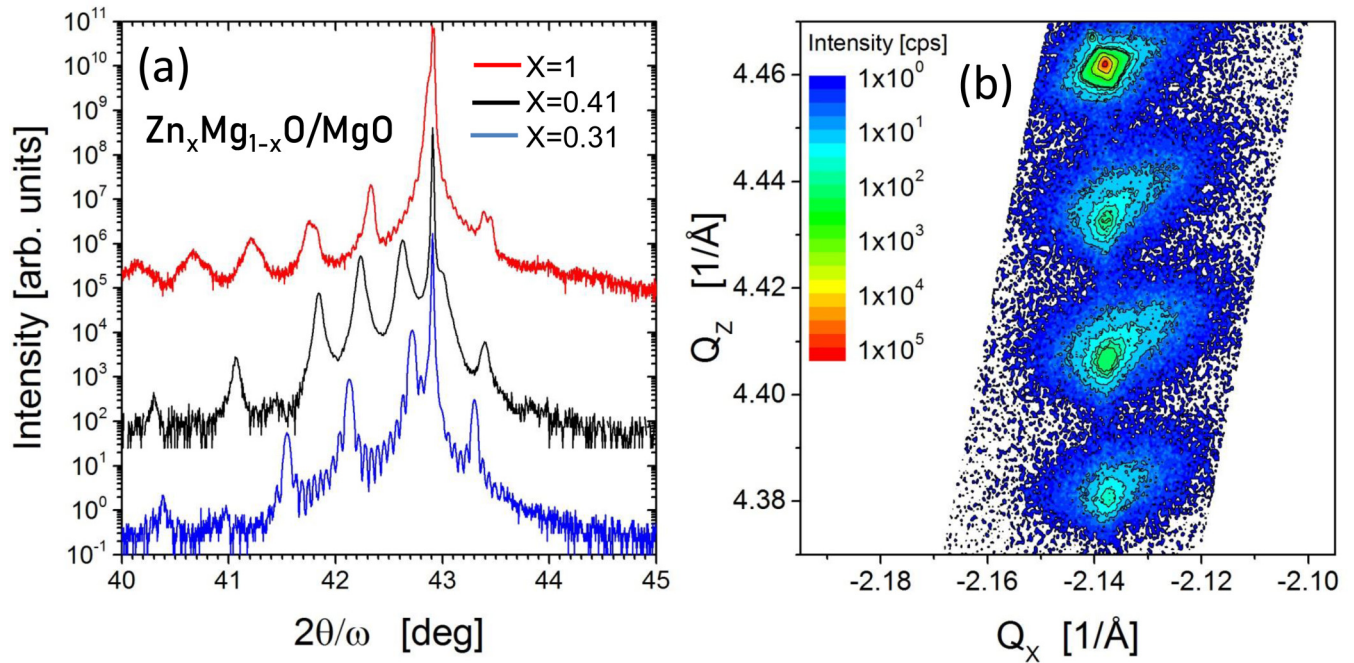
FIG. 7. (a) HRXRD 002 reflection, $2\theta/\omega$ scans for RS $10 \times \{Zn_xMg_{1-x}O/MgO\}$ MQWs. The curves are artificially spaced along the Y axis for a better visualization of the peaks and tiny oscillations from the total thickness of the MQWS. The strongest peak is from the MgO substrate. (b) Reciprocal space map for $-1-13$ reflection (Zn composition, $x = 0.41$). The nodes of the peaks have the same coordinate Q_x as MgO (highest point in the map), indicating that the structure is fully strained.

at lower energy than the band gap. In such case, optical data in Fig. 9 are more consistent with the random and uniform Zn distributions than the clustered one. Although emission and absorption are very strong in ZnMgO alloys, this optical feature is not an absolute indication of the direct nature of their band gaps. The reason is the breakdown of the k selection rule for interband optical transitions between localized carriers,

which become dipole allowed at first order in indirect bandgap semiconductors [63].

We have found that the VBM of RS ZnMgO is often flat, as a result of Zn contributions (see Fig. 4). According to the effective mass theory, the holes would then have a heavy mass and a compact wave function, which makes them more
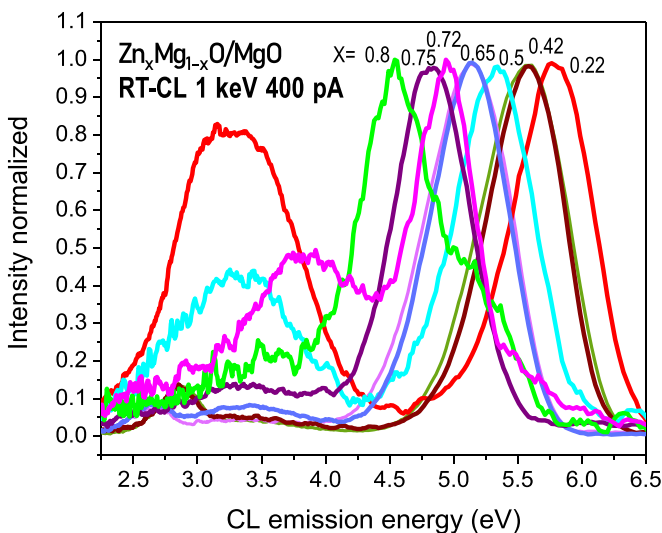

FIG. 8. CL measurements of RS $10 \times \{ZnMgO/MgO\}$ MQWs with different Zn concentrations. Two types of transitions are clearly visible: at lower energy (3–3.5 eV) and at the high energy (4–6 eV). All spectra are renormalized to have the same peak height.
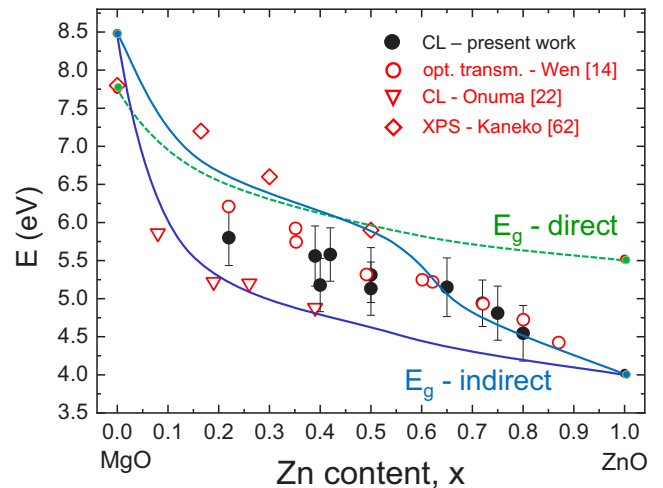

FIG. 9. Comparison of the theoretical band gaps (solid lines) and experimental data (symbols). CL measurements were performed in the present work and by Onuma *et al.* [22]. XPS measurements were performed by Kaneko *et al.* [60] and optical transmission spectra were obtained by Wen *et al.* [14]. Error bars correspond to CL FWHM.

sensitive to microscopic potential fluctuations. Therefore, in RS ZnMgO, fast localization of holes could be expected, followed by trapping of electrons and subsequent radiative recombination, which is very similar to the situation in InGaN alloys [52].

An interesting parallel can be drawn for nitride and oxide alloys by comparing the measured PL/CL FWHM and the maximal theoretical spread, ΔE_g, of the band gap due to the clustering effect:

$$\text{InGaN} : \text{FWHM} \sim 200 - 300 \, \text{meV}, \qquad \Delta E_g \sim 0.5 \, \text{eV}$$

$$\text{InAlN} : \text{FWHM} \sim 100 - 600 \, \text{meV}, \qquad \Delta E_g \sim 1.2 \, \text{eV}$$

$$\text{ZnMgO} : \text{FWHM} \sim 800 \, \text{meV (present work)}, \quad \Delta E_g \sim 1.3 \, \text{eV}$$

In the above scenario of hole localization, the fact that FWHM $\sim 0.4 - 0.6 \, \Delta E_g$ indicates that the hole wave function is quite compact, extending slightly beyond the nanometer scale of potential fluctuations in both nitrides and oxide alloys.

The observed effects (band-gap fluctuations, flattening of the highest valence band, high exciton binding energy, and strong electron-phonon coupling) could indicate an excitonic mechanism allowing indirect transitions for absorption and emission processes.

VI. SUMMARY AND CONCLUSIONS

The band structure calculations of RS $Zn_xMg_{1-x}O$ alloys were performed for various compositions and arrangements of Zn atoms, and the mechanisms of the band-gap fluctuations, Zn clustering, and direct-indirect gap transitions were explained on the basis of analysis of chemical origins of states at VBM. Our results led to the following conclusions:

(i) The calculated band-gap values in RS $Zn_xMg_{1-x}O$ strongly fluctuate depending on the mutual positions of substitutional Zn atoms. The largest spreads (up to 1.27 eV) of the band-gap values for the chosen composition x were achieved in the range of $0.1 < x < 0.6$. The mechanism of fluctuations can be explained by the formation of Zn clusters. In clustered configurations, Zn-Zn interactions through oxygen bridges lead to the smallest band gaps, while very dispersed Zn atom arrangements in uniform configurations lead to the largest gaps. The source of these effects is the VBM orbital structure. The clustered Zn-O-Zn configurations add the largest contributions to the Hamiltonian matrix through mixed ionic-covalent bonds between the p orbitals of O and $sp3d2$ Zn hybridization lobes, and also form banana bonds of the σ type between neighboring Zn. In the presence of these strong interactions, VBM is "pushed up," separating from the lower-energy bands, mainly of MgO origin, and reducing the fundamental band gap. This mechanism is very similar to the In clustering in nitride alloys [35].

(ii) Direct band gap (Γ-Γ) rarely occurs and only in some cases with $x < 0.5$, for atomic configurations in which Zn atoms are uniformly distributed in all crystal directions, avoiding Zn-O-Zn bridges.

(iii) Depending on the case, the VBM occurs at the X, M, R, and rarely at the Γ symmetry point or in its vicinity. Valence bands are sensitive to both short- and long-range Zn-Zn interactions, often changing shape and often being flat.

The latter property is a sign of strong electronic correlations and is closely related to the high thermoelectric power in these alloys due to the high density of states at the edge of the valence band [64].

(iv) Flattening of the valence band results in heavier effective mass and more compact wave functions of holes, favoring their localization in potential fluctuations that naturally occur in alloys on the nanometer scale, "even in the homogeneous random alloy" [52]. In RS ZnMgO alloys, this localization of the carrier (hole) is particularly marked due to the large energy spreading ($\Delta E_g > 1$ eV) caused by Zn clustering. An interesting correlation was found between the CL/PL line broadening FWHM and the maximal spread ΔE_g of the band gap due to the clustering effect, i.e., FWHM$\sim$0.4–0.6 ΔE_g, in ZnMgO, InAlN, and InGaN, confirming the hole compactness in these alloys.

(v) CL bands of our RS ZnMgO MQWs, as well as other optical band gaps reported in the literature, are within two theoretical limits of indirect band gaps and below ($>$0.5 eV) the lowest direct band gaps. However, at this stage, the effect of the carrier localization in these alloys makes it impossible to clearly identify their direct or indirect nature of the band gap, despite the strong emission and absorption properties.

Finally, it is worth mentioning that hexagonal BN (h-BN), an indirect and wide band-gap semiconductor, is very effective as a light emitting material. Recently, it has been measured that the photoluminescence (PL) intensity of a few h-BN layers is almost 100 times stronger than the intensity of a commercial 4-μm-thick AlN layer [65,66]. Such high efficiency of PL can be related to two factors: strong electron-phonon coupling (Fröhlich interaction) and high exciton binding energy (128 $\pm$ 15 meV for h-BN) [67,68]. In the case of MgO, the calculated exciton binding energy is 85 $\pm$ 10 meV [69], and electron-phonon coupling is also strong due to the highly ionic character of atomic bonds. Both of the above effects and the fact that we are dealing with alloys that favor the exciton trapping and radiative recombination in local potential fluctuations can make the indirect band gap in RS MgO/ZnMgO system visible in the CL experiments.

To summarize, our theoretical and experimental approach has shown that hole localization is strongly favored in RS ZnMgO as a result of flattening of the VBM by both short-range and long-range Zn-Zn interactions. Combined with the high exciton binding energy, these alloys can feature strong optical properties, even if their band gap could be indirect, making them an attractive and cost-effective candidate for deep-UV optoelectronic applications, such as water purification, sterilization (surface, food, etc.), or secure communications (non–line of sight). As the final conclusion resulting from our theoretical and experimental approach we can say that as the importance of UV emitters is increasing rapidly, the considered materials may become a second path to achieve the goal of having economic and practical sources of highly energetic light.

[1] X. Fang, Y. Bando, U. K. Gautam, T. Zhai, H. Zeng, X. Xu, M. Liao, and D. Golberg, Solid State Mater. Sci. **34**, 190 (2009).

[2] Y. Zou, Y. Zhang, Y. Hu, and H. Gu, Sensors **18**, 2072 (2018).

[3] C. B. Jacobs, A. B. Maksov, E. S. Muckley, L. Collins, M. Mahjouri-Samani, A. Ievlev, C. M. Rouleau, J.-W. Moon, D. E. Graham, B. G. Sumpter, and I. N. Ivanov, Sci. Rep. **7**, 6053 (2017).

[4] E. Fortunato, P. Barquinha, A. Pimentel, A. Goncalves, A. Marques, L. Pereira, and R. Martins, Thin Solid Films **487**, 205 (2005).

[5] S. Bai, W. Wu, Y. Qin, N. Cui, D. J. Bayerl, and X. Wang, Adv. Funct. Mater. **21**, 4464 (2011).

[6] X. Yang, C.-X. Shan, Y.-J. Lu, X.-H. Xie, B.-H. Li, S.-P. Wang, M.-M. Jiang, and D.-Z. Shen, Opt. Lett. **41**, 685 (2016).

[7] Ü. Özgür, Y. I. Alivov, C. Liu, A. Teke, M. A. Reshchikov, S. Doğan, V. Avrutin, S.-J. Cho, and H. Morkoç, J. Appl. Phys. **98**, 041301 (2005).

[8] X. S. Fang and L. D. Zhang, J. Mater. Sci. Technol. **22**, 1 (2006).

[9] S. Choopun, R. D. Vispute, W. Yang, R. P. Sharma, T. Venkatesan, and H. Shen, Appl. Phys. Lett. **80**, 1529 (2002).

[10] Y. Saeed, A. Shaukat, N. Ikram, and M. Tanveer, J. Phys. Chem. Solids **69**, 1676 (2008).

[11] M. Kurth, P. C. J. Graat, and E. J. Mittemeijer, Thin Solid Films **500**, 61 (2006).

[12] E. Ruiz, S. Alvarez, and P. Alemany, Phys. Rev. B **49**, 7115 (1994).

[13] C.-Y. J. Lu, Y.-T. Tu, T. Yan, A. Trampert, L. Chang, and K. H. Ploog, J. Chem. Phys. **144**, 214704 (2016).

[14] M. C. Wen, S. A. Lu, L. Chang, M. M. C. Chou, and K. H. Ploog, J. Cryst. Growth **477**, 169 (2017).

[15] D. Welch, M. Buonanno, V. Grilj, I. Shuryak, C. Crickmore, A. W. Bigelow, G. Randers-Pehrson, G. W. Johnson, and D. J. Brenner, Sci. Rep. **8**, 2752 (2018).

[16] Y. Taniyasu, M. Kasu, and T. Makimoto, Nature **441**, 325 (2006).

[17] *III-Nitride Ultraviolet Emitters-Technology and Applications*, edited by M. Kneissl and J. Rass, Springer Series in Materials Science (Springer, Berlin, 2016).

[18] J. E. Jaffe, R. Pandey, and A. B. Kunz, Phys. Rev. B **43**, 14030 (1991).

[19] V. S. Stepanyuk, A. Szász, B. L. Grigorenko, O. V. Faberovich, and A. A. Katsnelson, Phys. Status Solidi B **155**, 179 (1989).

[20] A. Djelal, K. Chaibi, N. Tari, K. Zitouni, and A. Kadri, Superlattices Microstruct. **109**, 81 (2017).

[21] J. Wang, Y. Tu, L. Yang, and H. Tolner, J. Comput. Electron. **15**, 1521 (2016).

[22] T. Onuma, M. Ono, K. Ishii, K. Kaneko, T. Yamaguchi, S. Fujita, and T. Honda, Appl. Phys. Lett. **113**, 061903 (2018).

[23] N. Marzari and D. Vanderbilt, Phys. Rev. B **56**, 12847 (1997).

[24] I. Souza, N. Marzari, and D. Vanderbilt, Phys. Rev. B **65**, 035109 (2001).

[25] A. Zunger, S.-H. Wei, L. G. Ferreira, and J. E. Bernard, Phys. Rev. Lett. **65**, 353 (1990).

[26] S.-H. Wei, L. G. Ferreira, J. E. Bernard, and A. Zunger, Phys. Rev. B **42**, 9622 (1990).

[27] V. Popescu and A. Zunger, Phys. Rev. Lett. **104**, 236403 (2010).

[28] J. P. Perdew and A. Zunger, Phys. Rev. B **23**, 5048 (1981).

[29] D. M. Ceperley and B. J. Alder, Phys. Rev. Lett. **45**, 566 (1980).

[30] G. Kresse and J. Furthmüller, Comput. Mater. Sci. **6**, 15 (1996).

[31] H. J. Monkhorst and J. D. Pack, Phys. Rev. B **13**, 5188 (1976).

[32] O. K. Andersen, Phys. Rev. B **12**, 3060 (1975).

[33] M. Methfessel, C. O. Rodriguez, and O. K. Andersen, Phys. Rev. B **40**, 2009 (1989).

[34] N. E. Christensen, Phys. Rev. B **30**, 5753 (1984).

[35] I. Gorczyca, T. Suski, N. E. Christensen, and A. Svane, J. Phys. C **30**, 063001 (2018).

[36] I. Gorczyca and N. E. Christensen, Physica B (Amsterdam, Neth.) **185**, 410 (1993).

[37] N. E. Christensen and I. Gorczyca, Phys. Rev. B **50**, 4397 (1994).

[38] I. Gorczyca, S. P. Łepkowski, T. Suski, N. E. Christensen, and A. Svane, Phys. Rev. B **80**, 075202 (2009).

[39] I. Gorczyca, T. Suski, N. E. Christensen, and A. Svane, Appl. Phys. Lett. **101**, 092104 (2012).

[40] G. Staszczak, I. Gorczyca, T. Suski, X. Q. Wang, N. E. Christensen, A. Svane, E. Dimakis, and T. D. Moustakas, J. Appl. Phys. **113**, 123101 (2013).

[41] S. P. Łepkowski, I. Gorczyca, K. Stefanska-Skrobas, N. E. Christensen, and A. Svane, Phys. Rev. B **88**, 081202(R) (2013).

[42] A. Svane, N. E. Christensen, I. Gorczyca, M. van Schilfgaarde, A. N. Chantis, and T. Kotani, Phys. Rev. B **82**, 115102 (2010).

[43] I. Gorczyca, K. Skrobas, T. Suski, N. E. Christensen, and A. Svane, J. Appl. Phys. **118**, 075702 (2015).

[44] S.-H. Wei, X. Nie, I. G. Batyrev, and S. B. Zhang, Phys. Rev. B **67**, 165209 (2003).

[45] P. Carrier and S.-H. Wei, J. Appl. Phys. **97**, 033707 (2005).

[46] D. Segev, A. Janotti, and C. G. Van de Walle, Phys. Rev. B **75**, 035201 (2007).

[47] N. Marzari, A. A. Mostofi, J. R. Yates, I. Souza, and D. Vanderbilt, Rev. Mod. Phys. **84**, 1419 (2012).

[48] G. H. Wannier, Phys. Rev. **52**, 191 (1937).

[49] A. A. Mostofi, J. R. Yates, Y. S. Lee, I. Souza, D. Vanderbilt, and N. Marzari, Comput. Phys. Commun. **178**, 685 (2008).

[50] P. Giannozzi, S. Baroni, N. Bonini, M. Calandra, R. Car, C. Cavazzoni, D. Ceresoli, G. L. Chiarotti, M. Cococcioni, I. Dabo *et al.*, J. Phys.: Condens. Matter **21**, 395502 (2009).

[51] M. P. Molepo and D. P. Joubert, Phys. Rev. B **84**, 094110 (2011).

[52] P. R. C. Kent and A. Zunger, Appl. Phys. Lett. **79**, 2339 (2001).

[53] W. Hahn, J.-M. Lentali, P. Polovodov, N. Young, S. Nakamura, J. S. Speck, C. Weisbuch, M. Filoche, Y.-R. Wu, M. Piccardo, F. Maroun, L. Martinelli, Y. Lassailly, and J. Peretti, Phys. Rev. B **98**, 045305 (2018).

[54] A. Janotti, D. Segev, and Ch. G. Van de Walle, Phys. Rev. B **74**, 045202 (20016).

[55] J. J. Meléndez and M. Wierzbowska, J. Phys. Chem. C **120**, 4007 (2016).

[56] F. A. Carey and R. J. Sundberg, *Advanced Organic Chemistry* (Springer, Berlin, 1977).

[57] N. Marzari and D. Vanderbilt, in *The 5th Williamsburg Workshop on First-Principles Calculations for Ferroelectrics*, AIP Conf. Proc. No. 436 (AIP, Melville, NY, 1998), p. 146.

[58] L. Pauling, J. Am. Chem. Soc. **53**, 1367 (1931).

[59] https://www.nobelprize.org/prizes/chemistry/1976/summary/.

[60] K. Kaneko, T. Onuma, K. Tsumura, T. Uchida, R. Jinno, T. Yamaguchi, T. Honda, and S. Fujita, Appl. Phys. Express **9**, 111102 (2016).

[61] L. K. Wang, Z. G. Ju, C. X. Shan, J. Zheng, B. H. Li, Z. Z. Zhang, B. Yao, D. X. Zhao, D. Z. Shen, and J. Y. Zhang, J. Cryst. Growth **312**, 875 (2010).

[62] H. L. Liang, Z. X. Mei, Z. L. Liu, Y. Guo, A. Yu. Azarov, A. Yu. Kuznetsov, A. Hallen, and X. L. Du, Thin Solid Films **520**, 1705 (2012).

[63] C. Delerue, G. Allan, and M. Lannoo, Phys. Rev. B **48**, 11024 (1993).

[64] M. Wierzbowska and A. Dominiak, Carbon **80**, 255 (2014).

[65] D. A. Laleyan, K. Mengle, S. R. Zhao, S. R. Y. J. Wang, E. Kioupakis, and Z. T. Mi, Opt. Express **26**, 23031 (2018).

[66] L. Schue, L. Sponza, A. Plaud, H. Bensalah, K. Watanabe, T. Taniguchi, F. Ducastelle, A. Loiseau, and J. Barjon, Phys. Rev. Lett. **122**, 067401 (2019).

[67] G. Cassabois, P. Valvin, and B. Gil, Nat. Photonics **10**, 262 (2016).

[68] E. Cannuccia, B. Monserrat, and C. Attaccalite, Phys. Rev. B **99**, 081109(R) (2019).

[69] R. C. Whited and W. C. Walker, Phys. Rev. Lett. **22**, 1428 (1969).